Review of Scientific Instruments

RESEARCH ARTICLE | AUGUST 10 2026

Aerodynamic levitation for neutron scattering experiments on liquid droplets at high temperature

Phillip Eckstein ; Fan Yang ; Thomas C. Hansen ; Stanislav Savvin ; Jean-Marc Zanotti ; Quentin Berrod ; Andreas Meyer

Rev. Sci. Instrum. 97, 083303 (2026)
https://doi.org/10.1063/5.0341163

Review of Scientific Instruments ARTICLE pubs.aip.org/aip/rsi

Aerodynamic levitation for neutron scattering experiments on liquid droplets at high temperature

Cite as: Rev. Sci. Instrum. 97, 083303 (2026); doi: 10.1063/5.0341163
Submitted: 29 April 2026 • Accepted: 8 July 2026 •
Published Online: 10 August 2026

Phillip Eckstein,[1,a] Fan Yang,[1] Thomas C. Hansen,[2] Stanislav Savvin,[2] Jean-Marc Zanotti,[3] Quentin Berrod,[4] and Andreas Meyer[1,2]

AFFILIATIONS

[1] Institute for Frontier Materials on Earth and in Space, Deutsches Zentrum für Luft- und Raumfahrt (DLR), Cologne 51147, Germany
[2] Institut Laue-Langevin (ILL), Grenoble 38000, France
[3] Université Paris-Saclay, Laboratoire Léon Brillouin (CEA-CNRS), Gif-sur-Yvette 91191, France
[4] Université Grenoble Alpes, CNRS, CEA, Grenoble INP, IRIG, SyMMES, Grenoble 38000, France

[a] **Author to whom correspondence should be addressed:** phillip.eckstein@dlr.de

ABSTRACT

We present the design and the performance of a compact aerodynamic levitation apparatus optimized for *in situ* neutron scattering investigations of high-temperature liquids. This system addresses the critical challenge of low scattering volumes in containerless processing by enabling the stable levitation of large metallic and oxide droplets up to 4 mm in diameter. The device features a dual-sided CO_2 laser heating configuration that minimizes axial thermal gradients, ensuring a homogeneous temperature throughout the sample. To achieve an exceptional signal-to-background ratio, the device employs a sophisticated neutron shielding concept for masking and a novel chamber geometry that effectively suppresses undesired Bragg scattering. Furthermore, a modular system of variable nozzle geometries and materials provides the device's adaptability to diverse sample classes ranging from metallic glass-formers to oxides applicable to a variety of scattering techniques. The capabilities of the apparatus are validated through neutron diffraction and time-of-flight spectroscopy experiments at the Institut Laue–Langevin. We report first results on the static structure factors of Pd–Ni–S melts, the atomic dynamics of supercooled Pd–Cu–Ni–P glass-formers, and the time-resolved crystallization behavior of lunar regolith simulants.

I. INTRODUCTION

Containerless levitation is a highly effective technique for processing reactive materials, enabling the study of metastable and undercooled liquids without contamination, particularly at elevated temperatures. This approach offers a unique solution by avoiding contact of the sample material with container walls. It thereby prevents chemical interactions between the crucible and the sample that could alter or contaminate the material, which is a typical problem in conventional furnaces.[1–3] In addition, containerless levitation enhances accessibility for measurement tools, such as cameras and pyrometers, providing an undisturbed view on the sample and allows for investigations across extended temperature ranges.[2] This includes studying deeply undercooled liquids, as heterogeneous nucleation at the container wall can be avoided,[4] as well as materials at extremely high temperatures exceeding 2000 K.[5] These advantages make it an ideal platform for neutron and x-ray scattering experiments, providing an improved signal-to-noise ratio without scattering contributions from crucible materials and, thus, offering a powerful opportunity to investigate the atomic structure and dynamics of melts. Several containerless levitation methods have been applied for the characterization of liquid materials,[6] including electrostatic levitation (ESL),[7,8] electromagnetic levitation (EML),[9,10] acoustic levitation (AL),[11] aerodynamic levitation

(ADL),[12] and hybrid techniques combining multiple methods, such as electrostatic-aerodynamic levitation (ES-ADL).[13] Each method offers distinct advantages and limitations.

ESL is the preferred technique for containerless processing of metallic samples. It uses electric fields to levitate charged samples, with position control achieved through electrodes placed a few millimeters above and below the sample. This method allows for the stable levitation of samples up to 6 mm in diameter, fully visible without obstruction from surrounding equipment.[14] Heating is provided by lasers in a high-vacuum environment. However, metals containing high-vapor-pressure elements may undergo evaporation in vacuum, causing not only compositional changes but also uncontrolled electron loss that results in positional instability.[15] This instability represents a critical failure mode in multiphase systems, where the coexistence of distinct solid phases can induce sudden charge loss during phase transitions, which restricts the range of processable material systems.

EML enables the levitation of large samples, up to 8 mm in diameter, by utilizing magnetic fields to induce currents in electrically conductive materials.[16] The magnetic force, which is proportional to the applied current, allows for simultaneous levitation and inductive heating, providing precise temperature control. However, this coupling also limits the lowest possible temperature and the highest cooling rate.[17,18] While the copper coil system is essential for levitation and heating, it partially obstructs the sample's visibility.

AL uses acoustic waves generated by a resonant plate for levitating the samples. The waves have to be strong enough to counteract gravity, which makes this method suitable for less dense samples of smaller masses.[19,20]

Hybrid techniques, such as ES-ADL, offer a versatile approach by initially suspending the sample with a gas stream before gradually increasing the electric field until it fully maintains levitation. This method leverages the advantages of both techniques, enabling greater flexibility in sample handling. While it requires a more complex experimental setup combining the two methods, it provides enhanced control over levitation conditions. However, it still inherits mentioned limitations associated with conventional ESL regarding evaporation of elements with high vapor pressure.[21]

ADL utilizes a directed gas stream to suspend spherical samples based on the Bernoulli effect.[22,23] The levitation force is purely mechanical and independent of the sample's thermal or electromagnetic properties. This technique is characterized by its inherent simplicity, compact design, and versatile applicability across a range of experimental configurations. In contrast to the above mentioned levitation techniques, it offers the significant advantage of processing an extensive array of high-temperature and reactive metallic and oxide liquids,[24–26] in the equilibrium melt and the supercooled liquid state several 100 K below the melting point,[27] thereby affirming its efficacy as a containerless method. Heating is fully decoupled from the levitation state via a laser-based system, facilitating precise control of cooling rates. Furthermore, by operating at ambient pressure within a controlled atmosphere, ADL can prevent the rapid evaporation of volatile components, making it superior to vacuum-based techniques for specific classes of materials. However, the gas flow used for levitation introduces thermal gradients, which can be minimized through secondary laser heating from below, ensuring a more uniform temperature distribution.[28] In neutron scattering experiments, the inherently limited incident flux requires a sufficient scattering volume between the beam and the specimen to achieve statistically significant results. Consequently, when processing smaller samples, long acquisition times are necessary to obtain high-quality data. However, for metallic samples, such extended durations represent a critical challenge as metals are highly susceptible to oxidation at elevated temperatures. This oxidation not only compromises the chemical integrity of the material but may also destabilize the levitation. Surface irregularities resulting from oxide formation act as windage for the gas stream, inducing uncontrolled rotation and oscillation that can lead to potential nozzle contact. To mitigate these risks, the capability to levitate larger samples is required. By increasing the sample diameter, the interaction volume is significantly enhanced, leading to higher signal intensities and a substantial reduction in counting times, thereby minimizing the oxidation risk.

Previously, ADL combined with laser heating was employed in neutron scattering experiments on metallic samples, typically restricted to diameters of ~2.7 mm.[23] Kozaily *et al.* demonstrated the levitation of oxide samples up to 4 mm in diameter in quasi-elastic neutron scattering (QENS) experiments.[29] However, lower density materials, such as oxides, exhibit superior levitation stability because they require significantly lower gas flow rates compared to higher density metallic melts minimizing aerodynamic instabilities. Furthermore, the inherent resistance of oxides to high-temperature oxidation ensures long-term positional consistency and permits extended acquisition times. Conversely, the higher density of metallic systems necessitates increased gas flow to support the higher mass. In addition, the high susceptibility of metals to oxidation, which can compromise chemical integrity and destabilize levitation, requires an optimized setup. To address this, we present an aerodynamic levitation device developed for the stable processing of dense metallic spheres up to 4 mm in diameter, which is shown in Fig. 1. This significant increase in scattering volume, combined with the enhanced sensitivity of modern neutron detectors and increased neutron flux of instruments in the last decade, allows for rapid data acquisition and provides new possibilities to study these sample systems. The core of our development is not merely the construction of another levitator, but the combination of a precisely controlled atmosphere and an optimized heating design. Our system is engineered as "plug-and-play" device allowing for rapid integration and operation through an integrated centering mechanism, that is especially attractive for multi-user facilities. To mitigate the thermal gradients inherently induced by the gas flow, our setup utilizes dual-side heating. Furthermore, the purity of the sample environment has been optimized such that the oxygen concentration of the chamber atmosphere consistently remained below the 0.1% lower detection limit of the installed oxygen sensor during operation.

The levitator has been successfully tested at the European High Flux Neutron Source Institut Laue-Langevin (ILL), where *in situ* diffraction was performed at the D20 diffractometer,[30] alongside measurements at the XtremeD diffractometer[31] and QENS experiments at SHARPER time-of-flight inelastic spectrometer,[32] demonstrating its versatility for both structural and dynamical investigations of complex melts, such as Pd–Ni–S, Pd–Cu–Ni–P, and lunar regolith.

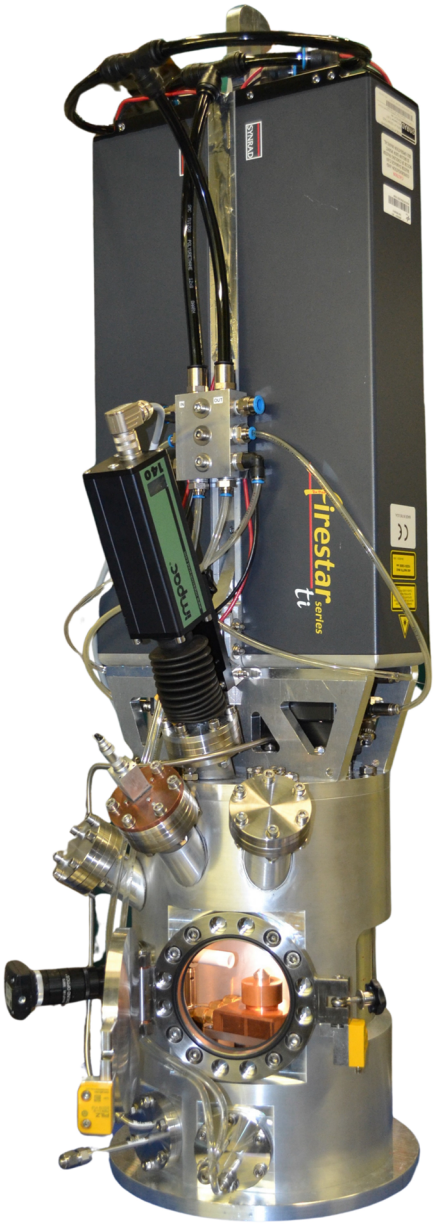

FIG. 1. Overview of the aerodynamic levitation apparatus. The upper assembly features two CO_2 lasers for sample heating, while the lower section displays the open levitation chamber with a direct view on the levitation nozzle. The visible attachments include a pyrometer (center, green/black) and a camera (left, black). The total height of the system is 1.12 m.

II. THE LEVITATION APPARATUS

The levitator setup is based on the fundamental principles described by Landron *et al.*,[22] Langstaff *et al.*[28], and Hennet *et al.*.[23] Designed for mobile and flexible use in multi-user facilities, the compact apparatus measures 1120 mm in height and 315 mm in width. A dedicated centering mechanism at the baseplate ensures that the center of the levitation chamber is automatically aligned with the incident beam and the instrument geometry, allowing for rapid installation and operation. Engineered as a fully integrated system, it features a complete set of pre-installed diagnostic and control components, allowing for short setup time by requiring only standard connections for cooling water, electricity, and levitation gas.

The vacuum-tight aluminum chamber is constructed from a low-scattering aluminum alloy with a diameter of 250 mm to reduce parasitic scattering from the chamber walls and minimal radioactive activation during neutron experiments. It features multiple (vacuum) view ports for diagnostic tools, optical access, and atmosphere control, with sample exchange facilitated through a DN 100 CF door. To achieve an exceptional signal-to-background ratio, in addition to the chamber design described above, the apparatus utilizes a shielding system made of neutron-absorbing boron enriched carbide material (Mirrobor-H^{TM}) to effectively suppress incoherent and stray scattering contributions. The incoming neutron beam enters the chamber through a 2 mm thick aluminum window and is guided by a boron nitride pipe through a 5 mm diameter pinhole aperture (PH) positioned directly in front of the sample, which is tilted at 45° to the incident beam, away from the detectors, to ensure that high-angle scattered neutrons reach the detectors while minimizing aperture scattering. A boron nitride "get-lost" pipe captures the primary beam behind the sample, supplemented by a beamstop. This configuration provides an unshaded horizontal scattering angle of 160° (between min. 7° and max. 167°) and a vertical range of 20°, as depicted light purple in Figs. 2 and 3.

To prevent oxidation of reactive metallic melts and reduce scattering from the chamber atmosphere, ultrahigh-purity argon 6.0 (<0.5 ppm O_2) is used as levitation gas and for purging the 12-l cylindrical chamber with oxygen levels monitored by an analyzer. However, metallic samples of high masses require elevated gas flow rates up to 1 l min^{-1} to be suspended with this setup. Under these dynamic flow conditions, the oxygen concentration within the chamber continuously remained below 0.1%, which defines the physical lower limit of detection for the installed oxygen sensor. Given the high purity of the inlet gas supply, the actual oxygen partial pressure within the processing atmosphere is anticipated to be orders of magnitude lower than this instrumental detection limit. Still, the continuous gas throughput into the chamber can allow atmospheric ingress. To optimize gas consumption and eliminate this throughput-driven oxygen intake, a future upgrade will feature a gas circulation system with an integrated closed-loop gas purification system to continuously recirculate and re-purify the inert atmosphere.

Heating is provided by two 100 W CO_2 lasers (Synrad Firestar ti series) operating at a wavelength of 10.9 μm. The 2.2 mm diameter laser beams enter the chamber through infrared-transparent NaCl windows and are directed via gold-coated copper mirrors to heat the sample simultaneously from above and below, as shown in Fig. 2. This dual-beam configuration ensures a uniform temperature distribution and mitigates thermal gradients inherently caused by the cooling gas stream. To facilitate experiments in open experimental halls, the system operates under class 1 laser safety standards, managed by a three-stage interlock circuit comprising door monitoring, key activation, and shutter control. The optical alignment of the laser beams can be performed using a collinear diode laser and

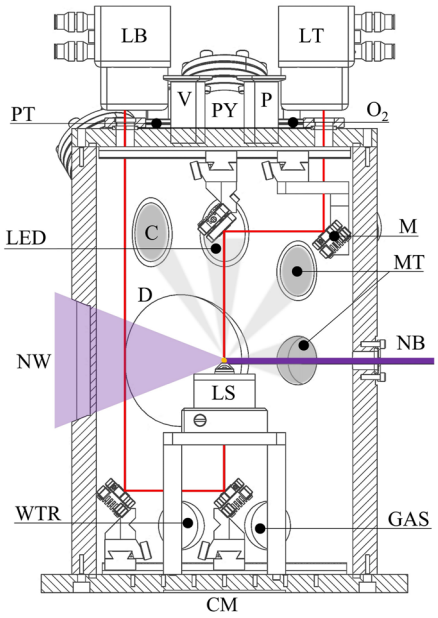

FIG. 2. Illustration of the levitation chamber with sectional view from the side, highlighting the ports for the respective measurement instruments and access points. For clarity, certain flanges and components of the shielding system have been omitted. LB: Laser bottom; LT: laser top; PT: pressure transmitter; O_2: oxygen sensor; V: magnetic valve; P: pump; PY: pyrometer; LED: chamber illumination by LED; M: one of the four equivalent mirrors; MT: empty, free port for additional equipment (e.g., for synchrotron or thermophysical property measurements and a future sample changer); C: camera; D: DN 100 CF access door; NB: incoming neutron beam (purple); NW: neutron window with vertical scattering angle of 40° indicated (transparent purple area); LS: levitator support; WTR: cooling water supply; GAS: gas inlet; CM: centering mechanism; red lines: deflected path of the laser beam; yellow area of a circle: sample.

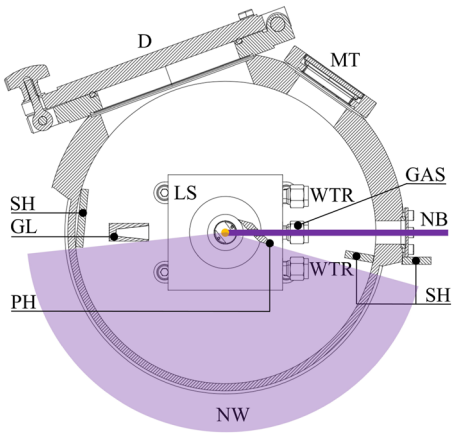

FIG. 3. Illustration of the levitation chamber with sectional view from top, highlighting significant parts. Certain components have been omitted for an improved overview. D: DN 150 CF access door; MT: empty, free port for additional equipment; NB: incoming neutron beam (purple); NW: neutron window with horizontal scattering angle of 160° indicated (transparent purple area); LS: levitator support; WTR: cooling water supply; GAS: gas inlet; SH: shielding; GL: "get-lost" pipe; PH: pinhole for shielding and neutron beam shaping. Yellow circle: sample.

micrometer screws to adjust the mirrors. Due to the fixed positioning of the lasers on top of the chamber, once aligned, the mirrors remain stable and require only periodic verification.

The temperature during processing is continuously monitored using a single-color pyrometer (Impac IGA 140 or IN 140) positioned diagonally above the nozzle outside the chamber. For the investigation of metallic melts, the IGA 140 model is utilized, featuring a spectral range of 1.45–1.8 μm and a measurement range of 300–2000 °C, whereas the IN 140 model is employed for oxides with a spectral range of 5.14 μm and a range of 500–2500 °C. Access to the sample is provided through an infrared-transparent CaF_2 window, allowing the pyrometer to record emitted radiation within a spot size of ~0.6 mm at a sampling rate of up to 100 Hz with a precision of ±1%.

The core of the system is the levitation nozzle as depicted in Fig. 4, which suspends spherical samples in a gas stream and allows the bottom laser access through a central opening. The levitation gas stream is directed through the nozzle orifice, impinging on the sample from below with sufficient force to counteract gravity. Precise gas flow is regulated by Brooks SLA5850 mass flow controllers in 1% increments at 10 Hz intervals delivering up to 2 l min^{-1}, maintaining levitation stability tailored to the respective size and mass of the sample. A defining feature of this apparatus is the nozzle modularity, designed for adapting to diverse sample properties and scattering techniques. Nozzle tips are fabricated with varying dimensions, including hole diameters (1.0–1.4 mm) and cone depths (2.0–3.0 mm). The hole diameter defines the sample surface area exposed to the primary gas stream and consequently the lifting force, while the cone depth determines the sample's levitation height relative to the nozzle's upper edge. The nozzle tip geometry features a 60° conical opening at the top to stabilize the sample and a 60° opening at the bottom to optimize gas collimation and laser reflection.[12,28,33] Material selection is equally critical and adapted to the specific neutron technique employed: For neutron diffraction, we utilize vanadium nozzles due to the small coherent neutron scattering length of the material, which simplifies data post-processing by allowing for the direct subtraction of the nozzle's diffraction intensity from the total signal. For spectroscopic applications, we have developed aluminum nozzles coated with a layer of boron, which effectively masks the nozzle structure by absorbing scattered neutrons, thereby significantly reducing background contributions. The entire nozzle assembly is mounted on a water-cooled copper stage to prevent overheating and sample adhesion, while the pedestal itself is constructed from boron-alloyed aluminum (Al-8 wt. %B) to provide high thermal conductivity while minimizing background scattering.

The levitator can also be adapted for synchrotron instruments, enabling *in situ* small- and wide-angle scattering measurements with minor modifications, as done in previous experiments by Greaves *et al.*.[34] Future upgrades include a second pyrometer for operando monitoring of thermal gradients through the bottom nozzle hole, an internal sample magazine to reload samples without breaking the argon atmosphere, and the mentioned gas circulation system. The latter may include an integration of a closed-loop gas purification system to maintain high purity of the atmosphere once the desired target level is achieved. By recirculating the inert gas through a purification stage, the total gas consumption is minimized while

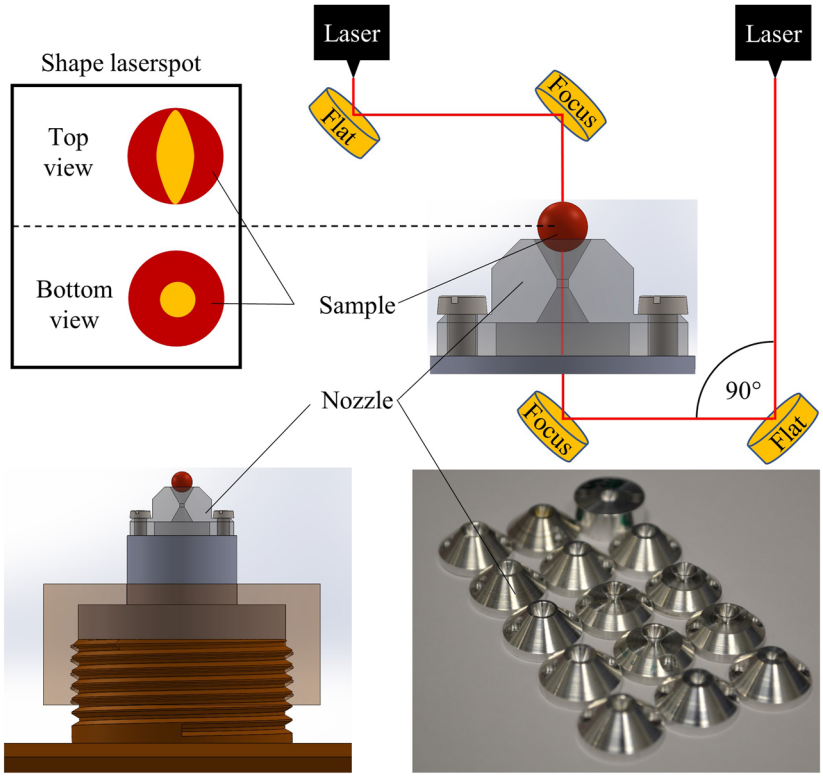

FIG. 4. Two lasers are directed toward the sample, with each beam being manipulated by a flat mirror and a focusing mirror. The laser beam approaching from below adopts the circular spot shape defined by the nozzle opening, while the beam from above forms its spot shape through the configuration of the mirror arrangement.

ensuring that the chemical integrity of the environment is preserved throughout the experiment.

Optimizing the signal-to-noise ratio requires a critical balance in gas flow regulation. Increasing the flow elevates the sample to maximize neutron beam exposure. However, the sample's lower hemisphere must remain sufficiently submerged within the nozzle cone to sustain the stabilizing Bernoulli effect.[35] By processing larger sample volumes, the scattering intensity is directly enhanced and, thus, the acquisition time reduced. While the maximum diameter is physically constrained by the melt's surface tension and its ability to resist deformation under gravitational and aerodynamic forces, neutron scattering tolerates minor geometric deviations provided that positional stability is maintained without nozzle contact.[33] This contrasts with thermophysical property measurements where perfect sphericity is often required.[36] It should be noted that while the system provides high stability for ideal spherical samples, surface irregularities or non-spherical geometries can induce significantly larger spatial deflections. However, datasets exhibiting such instabilities are typically discarded, as the resulting uncertainties in the interaction volume and scattering geometry render the measurements unusable for analysis.

A. Levitation stability and positioning

The precise alignment and stability of the levitated specimen are prerequisites for high-fidelity neutron diffraction and spectroscopy. In diffraction experiments, any deviation of the sample centroid from the calibrated center of the instrument introduces a shift in the effective scattering angle 2θ, resulting in a systematic error in the determination of the momentum transfer q. Furthermore, in time-of-flight experiments, any deviation from the nominal scattering center introduces an uncertainty in the neutron flight path to the detectors, which manifests as an artificial broadening of the energy resolution.

To minimize systematic errors, the apparatus relies on the mentioned centering mechanism whose static positioning accuracy is governed by the manufacturing tolerances of the interface (±0.3 mm) and the clearance fit required for the nozzle exchange, which introduces a maximum radial offset of ±0.5 mm. These geometric deviations of the device's center and so the sample's center from the nominal instrument center are compensated by adjusting the beam-line's slit system prior the measurement. This fine-tuning allows the neutron beam to be precisely shaped and aligned onto the actual position of the levitated specimen. However, during processing, dynamic instabilities may still arise, which can lead to rotation, induced oscillation, and potentially nozzle wall contact. To evaluate the dynamic stability of the levitated melt, a high-speed camera (HSC) was employed to record the sample under experimental conditions using the shadow-cast method.[37] A light source positioned behind the sample projected a shadow onto the camera lens. Using grayscale detection software, the sample's edge was identified by analyzing contrast changes along radial lines, allowing for the extrapolation of the complete ellipsoid even when the lower hemisphere was partially obstructed by the nozzle.[28] This analysis reveals a

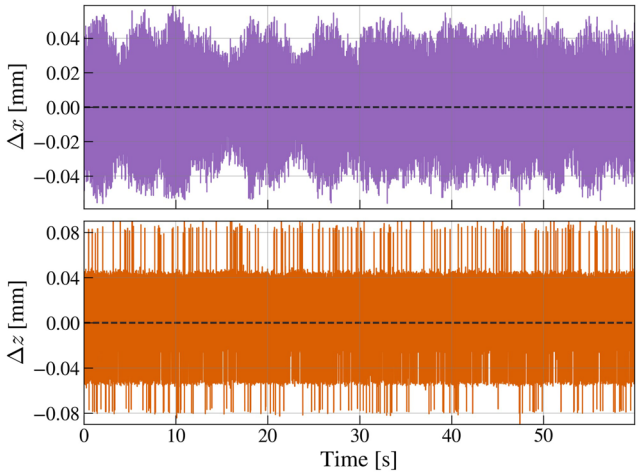

FIG. 5. Time-resolved trajectory of the center of mass coordinates of a sample with 4 mm diameter showing exemplary 1 min of lateral Δx (purple) and vertical Δz (orange) displacement. The centroid data were extracted via edge-detection algorithm fitting an ellipsoid to the visible upper hemisphere of the melt. The observed fluctuations indicate a confinement stability envelope of ≈±0.04 mm under equilibrium gas flow conditions.

relative positional stability of approximately Δx, Δz ≈ ±0.04 mm under typical processing conditions (Fig. 5), proving sufficient stability for the requirements of scattering experiments. Since the nozzle orifice is intrinsically aligned with the chamber's geometric center within the tolerances, the demonstrated confinement stability ensures that the sample is positioned at the instrument's scattering center upon docking the levitator via its base centering mechanism. The dynamic stability shown was validated across a broad parameter range of sample masses and nozzle geometries, ensuring that the levitation gas flow can be tailored to the specific density and surface tension of the melt. The observed positional fluctuations correspond to only 1% of a 4 mm sample diameter, resulting in a negligible uncertainty in the neutron flight path for spectroscopic measurements. For diffraction experiments, the deviation remains within acceptable limits as long as the primary beam continuously intersects the sample and does not partially miss it, thereby ensuring reliable data acquisition.

B. Temperature gradient

A critical challenge in the containerless processing of samples with dimensions in millimeter-scale is the minimization of thermal gradients. Historic single-point heating methods are known to generate significant axial temperature differentials, which can range from 100 K to over 1000 K depending on the material class and thermophysical properties.[38] To mitigate this, the presented apparatus employs a dual-sided laser heating configuration. While radiative losses ($\sim T^4$) at the lateral surfaces contribute to the temperature distribution, the "cold equator" effect is intensified by forced Marangoni convection as the cooling levitation gas accelerates through the narrow gap between the sample and the nozzle wall. This convective cooling, combined with radiative losses, inevitably creates thermal inhomogeneities. However, the application of laser energy from both the top and bottom poles restores symmetry to the thermal field. Literature on solid oxides, such as ZrO_2, demonstrates that such gradients can be drastically reduced from ~1000 K in single-sided setups to roughly 30 K when utilizing dual-sided heating combined with the inherent sample rotation.[39] In liquid samples, the situation may be even more favorable with respect to thermal homogeneity, as heat transport is not limited to conduction but is additionally enhanced by convective flow within the melt.

In the here presented setup, the localized laser heating theoretically creates temperature inhomogeneities. The top laser spot on the surface of the sample is shaped elliptically by the combination of flat and focused mirrors directing the beam each 90°, while the bottom spot on the sample surface appears circular, defined by the bottom nozzle hole, as the diameter of the hole is smaller than that of the laser spot, depicted in Fig. 4. Despite the different shape and size, particularly in the case of aluminum nozzles due to its high reflectivity to the laser's wavelength, the effective heating power reaching the sample's lower hemisphere exceeds the geometric limit of the orifice diameter due to multiple internal reflections of the laser beam within the nozzle channel. This channeling effect ensures that the heat flux remains comparable to that of the top laser, allowing for a symmetric 1:1 heating power ratio setting. However, when utilizing vanadium nozzles, an adjustment of this ratio may be necessary to compensate for the material's lower reflectivity.

The degree of thermal homogeneity is further governed by the fluid dynamics within the liquid drop, which differ fundamentally between material classes. Previous studies by Hennet *et al.* indicate that dual-sided heating is superior for maintaining stability and uniformity. This is particularly pronounced in metallic melts compared to oxides.[23] Oxide melts frequently exhibit high viscosities, which can dampen internal fluid motion. In contrast, the metallic melts investigated here (e.g., Pd–Ni–S) have significantly lower viscosities and higher thermal conductivities.[40] Due to the lower viscosity of the metal, this driving force facilitates a convection that aids in thermal redistribution, a mechanism that is often restricted in highly viscous oxides.

Another factor for the thermal homogeneity is the dynamic behavior of the sample. In our experiments, we observed that a reliable and vigorous rotation is established after the material has fully melted. In the liquid state, the surface tension forces are shaping the specimen into a sphere, eliminating mass imbalances and surface irregularities. The aerodynamic drag of the levitation gas stream induces a multi-axial rotation. This dynamic significantly mitigates the residual radial gradients. The continuous reorientation of the sample causes the laser impact zones to scan across the entire surface area, effectively averaging the heat load over the sample volume. The top panel of Fig. 6 illustrates the molten state of a 4 mm diameter metallic sample, which is stably levitated at ~1200 K and the lower panel provides a view of the optical components utilized to deflect the secondary laser beam for bottom heating.

C. Experimental procedure

To establish positional stability and ensure reproducible scattering geometries and material compositions during the high temperature processing, a protocol of material synthesis and geometric pre-shaping is executed. The experiments comprise distinct material classes, namely the ternary metallic glass-forming alloy

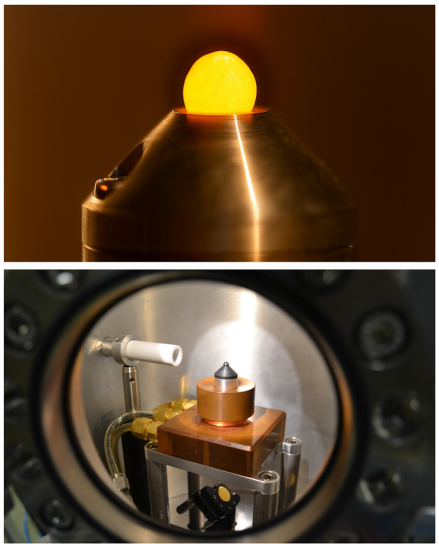

FIG. 6. The upper image displays a molten metallic sample levitating at ~1200 K above an aluminum nozzle. The lower image shows a view through the access door, revealing the water-cooled copper block for nozzle cooling and the guide for the incident neutron beam (white, left). A solid sample rests on a vanadium nozzle, while the secondary focusing mirror for the bottom laser is visible below.

melts $Pd_{40}Ni_{40}S_{20}$ and $Pd_{31}Ni_{42}S_{27}$, the multicomponent metallic melt $Pd_{43}Cu_{27}Ni_{10}P_{20}$ glass formers, and oxide lunar regolith simulants.

The Pd–Ni–S master alloys were synthesized by the Chair of Metallic Materials at Saarland University, following a specialized melting protocol to suppress sulfur evaporation and ensure stoichiometric precision.[41] Similarly, the Pd–Cu–Ni–P master alloys were prepared using a B_2O_3 fluxing technique to minimize oxide impurities, while the lunar regolith simulants were provided by the research consortium.[42] For the aerodynamic levitation experiments, the specimens were cut from these master alloys to a mass corresponding to a diameter of ~4 mm. The cut specimens are subsequently remelted in an arc furnace so that the surface tension of the liquid material naturally forms the irregular pieces into a spherical geometry, typically resulting in a flattened base at the point of crucible contact. In contrast to the metallic alloys, the lunar regolith simulants were preprocessed directly within the ADL. Here, the respective mass of the master material was melted in a specialized copper production nozzle using exclusively the top laser to achieve a spherical specimen of the required dimensions.

Prior to insertion into the levitator, samples are positioned on the nozzle orifice with this flattened base facing upward. This orientation ensures that the fully spherical lower hemisphere interacts with the levitation gas flow, maximizing hydrodynamic stability. Once the sample is loaded and the chamber sealed, a high-purity process atmosphere is established to prevent sample oxidation and minimize background scattering. The standard procedure involves evacuating the chamber to 10^{-4} mbar followed by purging with 6.0 argon by Linde, which is typically repeated twice. During operation, a magnetic valve regulates the outflow of the levitation gas to the vacuum pump to maintain a stable atmospheric pressure within the chamber. Levitation is initiated and sustained by regulating the argon mass flow via the controllers, with rates dynamically adjustable between 0 and 2 l min^{-1} depending on the specific mass and diameter of the sample. Once the sample position and the atmosphere in the chamber are stabilized, the laser heating is activated. The heating and cooling profile can be controlled manually or via pre-programmed sequences. A remote operation capability allows for precise control of the gas flow, laser output, and pyrometric monitoring from outside the radiation zone. Throughout the process, the sample temperature is continuously recorded.

III. RESULTS

To validate the performance of the newly developed ADL across varying scattering geometries and material classes, three distinct experimental campaigns were conducted at several instruments of the ILL neutron facility. The experiments were designed to test the limits of the apparatus regarding temperature stability, sample size, and signal-to-background ratio under real-time acquisition conditions. Beyond the primary scientific interest in these complex melts, these campaigns were used to evaluate and iteratively improve the performance of the system. We investigated the crystallization kinetics of oxide lunar regolith simulants on the diffractometer D20,[30] the atomic structure of the $Pd_{40}Ni_{40}S_{20}$ and $Pd_{31}Ni_{42}S_{27}$ alloys on the diffractometer XtremeD,[31] and the atomic dynamics of the $Pd_{43}Cu_{27}Ni_{10}P_{20}$ alloy using time-of-flight (ToF) spectroscopy on the SHARPER instrument.[32]

A. In-situ crystallization of lunar regolith

To validate the levitator's performance with oxide materials, experiments were conducted on anorthositic and basaltic lunar regolith simulants using the high-intensity two-axis diffractometer D20. A primary objective was to demonstrate that the reduced background signal of the new chamber design, combined with the flux of modern neutron diffractometers, enables the acquisition of statistically significant data within short integration times. Measurements were performed using a vanadium nozzle to minimize Bragg scattering contributions from the sample environment. The incident wavelength was set to $\lambda = 2.41$ Å. Unlike synchrotron radiation sources, the large beam cross section typical of neutron instruments illuminates the entire volume of the levitated droplet. This ensures that the resulting diffraction pattern represents the global state of the sample, including the onset of crystallization and phase separation in the bulk volume. The thermal protocol involved laser heating the samples to a fully liquid equilibrium state at 1675 K, followed by a controlled cooling ramp of 0.615 K s^{-1}. Due to the exceptional signal-to-background ratio, sample-specific scattering features were clearly resolvable within an integration time of only 120 s per spectrum.

Figure 7 presents a direct comparison of the diffraction patterns acquired at distinct thermal stages. The spectrum of the equilibrium melt exhibits the broad, diffuse appearance characteristic of a disordered liquid structure. Upon cooling, at 1365 K, sharp Bragg reflections emerge, indicating the onset of crystallization. The low background profile enables the resolution of even weak reflections during the cooling process. Observed peaks at ~4.3 $Å^{-1}$ are identified as likely attributable to magnetite (Fe_3O_4) and magnesium

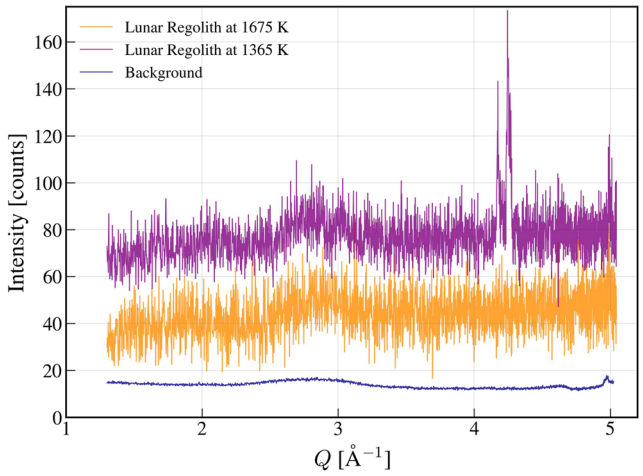

FIG. 7. Raw neutron scattering intensity (counts) of a lunar regolith sample (TUBS-M 50 wt. % orange glass) as a function of the scattering vector Q. The data compare the equilibrium melt at 1675 K with the diffraction pattern at 1365 K, which indicates the onset of crystallization during a constant cooling ramp of 0.615 K s^{-1}. For clarity of presentation, the 1365 K spectrum (purple curve) has been vertically offset by 40 counts. The background profile is shown in relation to the equilibrium melt (yellow curve) and illustrates the scattering contributions solely from the levitator vessel and the vanadium nozzle in the absence of a sample. Each *in situ* spectrum was recorded with an integration time of 120 s. The sharp features emerging at ~4.3 Å^{-1} in the 1365 K data correspond to crystalline Bragg reflections.

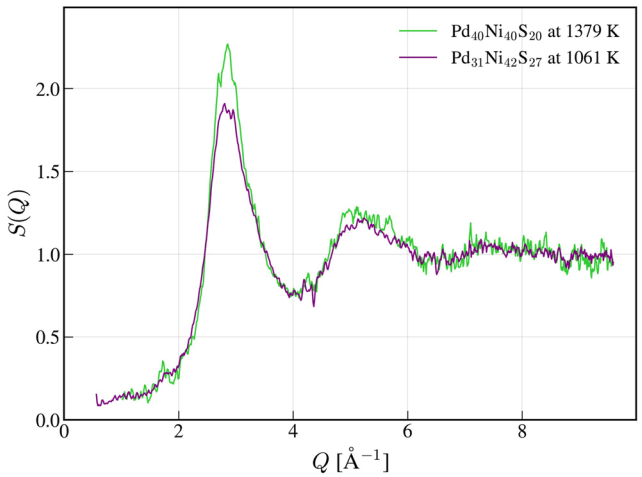

FIG. 8. Experimental total structure factors $S(Q)$ measured on the XtremeD diffractometer using ADL. The green curve displays the data for a $Pd_{40}Ni_{40}S_{20}$ melt at 1379 K, while the purple curve shows the $Pd_{31}Ni_{42}S_{27}$ alloy at 1061 K.

oxide (MgO). This temporal resolution allowed for the continuous, *in situ* observation of the transition from the amorphous liquid to the crystalline solid state.

B. Static structure of the Pd–Ni–S system

The ternary alloy Pd–Ni–S was selected to investigate the structural influence of sulfur in bulk metallic glass-forming liquids. Unlike the well-characterized Pd–Ni–P system, thermodynamic modeling and experimental studies of the melt dynamics indicate that the Pd–Ni–S system exhibits distinct glass-forming abilities and thermodynamic properties driven by the specific interactions of sulfur.[43] Recent QENS measurements reveal that sulfur-bearing melts display a decoupling of self-diffusion coefficients and melt viscosities, which deviate significantly from their phosphorus-based counterparts, suggesting a fundamental difference in the liquid structure.[44] The primary objective was to resolve the total static structure factor $S(Q)$ of the equilibrium liquid. Measurements were conducted using the wide-angle neutron diffractometer XtremeD, which is optimized for high neutron flux and small sample volumes, making it an ideal candidate for testing the ADL's capability to process dense metallic melts. The experiment utilized an incident neutron wavelength of $\lambda = 1.2$ Å to process the two alloy compositions $Pd_{40}Ni_{40}S_{20}$ and $Pd_{31}Ni_{42}S_{27}$.

Figure 8 illustrates the total structure factors $S(Q)$ obtained for the molten alloys. The instrument configuration allowed coverage up to $Q \approx 9.5$ Å^{-1}. It is possible to derive the extraction of distinct oscillation features in $S(Q)$ for $Pd_{40}Ni_{40}S_{20}$ at 1379 K, measured for 30 min, and $Pd_{31}Ni_{42}S_{27}$ at 1061 K, measured for 60 min. Both temperatures are above the respective melting points of the samples. Prior to structural analysis, raw intensities were corrected for background contributions from the levitation chamber and the nozzle as described in Sec. II. To isolate the coherent scattering signal, the data were corrected for absorption and multiple scattering and subsequently normalized to the composition-weighted average scattering cross section.

A comparison of the spectra demonstrates that variations in stoichiometry result in observable modifications to the structure factor. The difference in the broadening of the first peak and its amplitude indicates that the liquid structure is highly sensitive to the sulfur concentration. As sulfur content increases, a subtle shift in the position of the first maximum is observed, suggesting a reorganization of the local atomic packing and a change in the average interatomic distances within the short-range order. While the current work focuses on the validation of the containerless ADL setup, these results confirm its readiness for advanced experiments employing isotopic substitution (e.g., ^{58}Ni, ^{60}Ni) and complementary synchrotron x-ray diffraction to reveal more detailed information on the influence of sulfur on the chemical and topological ordering in the melt.

C. Relaxational dynamics in viscous Pd–Cu–Ni–P

Time-of-flight neutron spectroscopy was performed at the SHARPER spectrometer to investigate the atomic dynamics of the glass-forming liquid $Pd_{43}Cu_{27}Ni_{10}P_{20}$. This system is one of the metallic glass formers with the best glass-forming ability. Previous studies of the microscopic dynamics in this melt using quasi-elastic neutron scattering were performed for small q ranges and incoherent scattering due to the interference of crucible materials. A key technical advantage of the present ADL setup is the ability to use shorter incident wavelengths, without masking the signal with Bragg scattering from the sample environment close the structure factor maximum of the liquid at around 2.9 Å^{-1}, which limited measurements in conventional furnaces.

By eliminating the crucible used (Al_2O_3), we can now access the melt dynamics at the structure factor maximum $S(Q_0)$ near $q \approx 2.9$ Å^{-1}. This allows us to investigate the temperature and wave vector dependence of the microscopic relaxation time in the here used atomic model system. The measurements were performed with an incident wavelength of $\lambda = 3.5$ Å and a Fermi-chopper speed of 6263 rpm, providing an instrument energy resolution of approximately $\Delta E \approx 256$ μeV. The accessible momentum transfer range is $0.5 < q < 3.2$ Å^{-1}. The sample was measured at 5 different temperatures and room temperature: 855, 1010, 1041, 1063, and 1112 K with varying counting times between ~1 and 2 h, depending on the stability of the levitated sample. The experimental scattering intensities were normalized to the monitor signal to account for variations in incident neutron flux and acquisition time, while detector efficiency was corrected via normalization to a vanadium standard. Data were initially acquired as a function of neutron time-of-flight (TOF). These datasets were then converted to energy transfer $\hbar\omega$ and remapped into constant momentum transfer Q bins using the Mantid Workbench software.[45] This reduction process ensures that the resulting dynamic structure factors, as shown in Fig. 9, accurately represent the intrinsic atomic dynamics of the $Pd_{43}Cu_{27}Ni_{10}P_{20}$ melt.

It can be seen in Fig. 9 that at both showed temperatures, quasi-elastic broadening and, therefore, atomic dynamics in the sample can be observed. At the structure factor maximum, the background contribution from the empty levitator setup accounts for ~30% of the total signal at zero energy transfer, and of about 20% at a neutron energy transfer of about 0.5 meV. At the neutron energy loss side, an characteristic increase in intensity of empty levitator is observed, which could be attributed to residual scattering from the argon process atmosphere and multi-phonon contributions from the nozzle assembly. A first estimation of the structural relaxation time at $q = 2.9$ Å^{-1} gives 4 ± 1 ps at 1121 K. Together with the macroscopic thermophysical properties of the liquid like melt viscosity, the time and length scale dependent structural relaxation time allows the understanding of microscopic transport mechanism in the melt, and how it controls the macroscopic properties of the liquid. A comprehensive multi-scale investigation, integrating these structural and dynamical findings with macroscopic thermophysical properties, will be presented in subsequent publications.

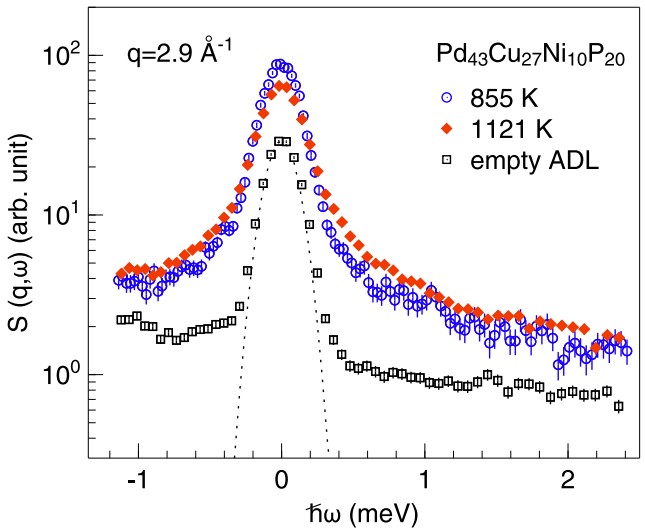

FIG. 9. Measured dynamic structure factors $S(Q, \omega)$ of the $Pd_{43}Cu_{27}Ni_{10}P_{20}$ glass-former at 855 K and at 1112 K. The data are compared against the scattering intensity of the empty ADL furnace. The spectra were recorded at a momentum transfer of $Q \approx 2.9$ Å^{-1}, which corresponds to the maximum of the static structure factor $S(Q_0)$ of the liquid. The dashed line represents the instrumental resolution function.

IV. CONCLUSION

In this paper, we presented the development and successful commissioning of a novel aerodynamic levitation system tailored for high-temperature neutron scattering experiments. The device enables the stable processing of large sample volumes up to 4 mm in diameter while maintaining a superior signal-to-background ratio through integrated shielding and an optimized, vacuum-tight chamber geometry. Thermal homogeneity is supported by a dual-sided CO_2 laser heating configuration that mitigates axial gradients, while maintaining the process atmosphere below the 0.1% oxygen sensor detection floor was sufficient to suppress oxidation in reactive melts over extended acquisition periods. Validated through *in situ* experiments with lunar regolith simulants, diffraction on Pd–Ni–S and time-of-flight spectroscopy on Pd–Cu–Ni–P, the device's modular nozzle system and "plug-and-play" centering mechanism provide a robust and versatile platform for investigating the structural and dynamical properties of complex liquids in multi-user facilities.

ACKNOWLEDGMENTS

We acknowledge the Institut Laue-Langevin for providing neutron beam time and the support of the author community. We thank the instrument scientists and technical support staff of the D20, XtremeD, and SHARPER beamlines, without whom the present work would not have been possible. We extend our sincere gratitude to Louis Hennet for his guidance and initial assistance in the development of the levitation assembly. Finally, we thank Jennifer Sutherland for providing the lunar regolith simulant samples, for her contributions to the D20 diffraction experiment and we thank the group Metallic Materials at Saarland University for the preparation of the Pd-Ni-S master alloys used in this study.

AUTHOR DECLARATIONS

Conflict of Interest

The authors have no conflicts to disclose.

Author Contributions

Phillip Eckstein: Conceptualization (lead); Data curation (equal); Formal analysis (equal); Investigation (equal); Methodology (lead); Software (equal); Validation (equal); Writing – original draft (lead); Writing – review & editing (equal). **Fan Yang**: Conceptualization (equal); Data curation (equal); Formal analysis (equal); Methodology (equal); Software (equal); Supervision (equal); Validation (equal); Writing – review & editing (equal). **Thomas C. Hansen**:

Investigation (equal); Methodology (supporting); Resources (supporting); Validation (supporting). **Stanislav Savvin**: Data curation (supporting); Formal analysis (supporting); Investigation (equal); Software (supporting); Validation (equal). **Jean-Marc Zanotti**: Investigation (equal); Methodology (supporting); Software (supporting); Validation (supporting). **Quentin Berrod**: Data curation (equal); Formal analysis (equal); Investigation (equal); Methodology (supporting); Software (equal); Validation (equal). **Andreas Meyer**: Conceptualization (supporting); Data curation (equal); Formal analysis (equal); Funding acquisition (lead); Investigation (equal); Methodology (supporting); Project administration (lead); Software (equal); Supervision (lead); Validation (equal); Writing – review & editing (equal).

DATA AVAILABILITY

The data that support this study are openly available at the ILL portal, D20, https://doi.org/10.5291/ILL-DATA.5-25-291;[46] XtremeD, https://doi.org/10.5291/ILL-DATA.6-05-1086;[47] and SHARPER, https://doi.org/10.5291/ILL-DATA.6-05-1097[48] for each beamtime. Raw data were generated at the ILL large scale facility. Derived data supporting the findings of this study are available from the corresponding author upon reasonable request.

REFERENCES

[1]Y. Bayazitoglu, P. V. R. Suryanarayana, and U. B. Sathuvalli, "High temperature thermal diffusivity determination procedure for solids and liquids," J. Thermophys. Heat Transfer **4**, 462–468 (1990).

[2]F. Shen, J. M. Khodadadi, M. C. Woods, J. K. R. Weber, and B. Q. Li, "Containerless thermal diffusivity determination of high-temperature levitated spherical specimen by extended flash methods: Theory and experimental validation," J. Heat Transfer **119**, 210–219 (1997).

[3]P. C. Nordine, J. K. R. Weber, and J. G. Abadie, "Properties of high-temperature melts using levitation," Pure Appl. Chem. **72**, 2127–2136 (2000).

[4]D. M. Herlach, R. F. Cochrane, I. Egry, H. J. Fecht, and A. L. Greer, "Containerless processing in the study of metallic melts and their solidification," Int. Mater. Rev. **38**, 273–347 (1993).

[5]L. B. Skinner, C. J. Benmore, J. K. R. Weber, M. A. Williamson, A. Tamalonis, A. Hebden, T. Wiencek, O. L. G. Alderman, M. Guthrie, L. Leibowitz, and J. B. Parise, "Molten uranium dioxide structure and dynamics," Science **346**, 984–987 (2014).

[6]L. Hennet, D. Holland Moritz, R. Weber, and A. Meyer, ""High-temperature levitated materials," in neutron scattering—Applications in biology, chemistry, and materials science," Exp. Methods Phys. Sci. **49**, 583–636 (2017).

[7]W.-K. Rhim, S. K. Chung, D. Barber, K. F. Man, G. Gutt, A. Rulison, and R. E. Spjut, "An electrostatic levitator for high-temperature containerless materials processing in 1-g," Rev. Sci. Instrum. **64**, 2961–2970 (1993).

[8]P.-F. Paradis, T. Ishikawa, and S. Yoda, "Electrostatic levitation furnace for structural studies of high temperature liquid metals by neutron scattering experiments," J. Non-Cryst. Solids **312–314**, 309–313 (2002).

[9]E. C. Okress, D. M. Wroughton, G. Comenetz, P. H. Brace, and J. C. R. Kelly, "Electromagnetic levitation of solid and molten metals," J. Appl. Phys. **23**, 545–552 (1952).

[10]G. Jacobs, I. Egry, K. Maier, D. Platzek, J. Reske, and R. Frahm, "Extended x-ray-absorption fine structure studies of levitated undercooled metallic melts," Rev. Sci. Instrum. **67**, 3683–3687 (1996).

[11]G. F. Mitchell, Y. Bayazitoglu, and R. Shampine, "Acoustically levitated droplet viscosity measurement," J. Thermophys. Heat Transfer **12**, 599–602 (1998).

[12]P. C. Nordine and R. M. Atkins, "Aerodynamic levitation of laser-heated solids in gas jets," Rev. Sci. Instrum. **53**, 1456–1464 (1982).

[13]P.-F. Paradis, T. Ishikawa, J. Yu, and S. Yoda, "Hybrid electrostatic–aerodynamic levitation furnace for the high-temperature processing of oxide materials on the ground," Rev. Sci. Instrum. **72**, 2811–2815 (2001).

[14]T. Kordel, D. Holland-Moritz, F. Yang, J. Peters, T. Unruh, T. Hansen, and A. Meyer, "Neutron scattering experiments on liquid droplets using electrostatic levitation," Phys. Rev. B **83**, 104205 (2011).

[15]P.-F. Paradis, T. Ishikawa, G.-W. Lee, D. Holland-Moritz, J. Brillo, W.-K. Rhim, and J. T. Okada, "Materials properties measurements and particle beam interactions studies using electrostatic levitation," Mater. Sci. Eng.: R Rep. **76**, 1–53 (2014).

[16]A. Meyer, S. Stüber, D. Holland-Moritz, O. Heinen, and T. Unruh, "Determination of self-diffusion coefficients by quasielastic neutron scattering measurements of levitated Ni droplets," Phys. Rev. B **77**, 092201 (2008).

[17]T. Schenk, D. Holland-Moritz, V. Simonet, R. Bellissent, and D. M. Herlach, "Icosahedral short-range order in deeply undercooled metallic melts," Phys. Rev. Lett. **89**, 075507 (2002).

[18]D. Holland-Moritz, T. Schenk, P. Convert, T. Hansen, and D. M. Herlach, "Electromagnetic levitation apparatus for diffraction investigations on the short-range order of undercooled metallic melts," Meas. Sci. Technol. **16**, 372–380 (2005).

[19]Y. Bayazitoglu and G. Mitchell, "Surface tension measurements of acoustically levitated droplets," in *National Heat Transfer Conference* (American Institute of Aeronautics and Astronautics, Reston Virigina, 1995).

[20]J. K. R. Weber, C. A. Rey, J. Neuefeind, and C. J. Benmore, "Acoustic levitator for structure measurements on low temperature liquid droplets," Rev. Sci. Instrum. **80**, 083904 (2009).

[21]T. Ishikawa, J. Yu, and P.-F. Paradis, "Noncontact surface tension and viscosity measurements of molten oxides with a pressurized hybrid electrostatic-aerodynamic levitator," Rev. Sci. Instrum. **77**, 053901 (2006).

[22]C. Landron, L. Hennet, J.-P. Coutures, T. Jenkins, C. Alétru, N. Greaves, A. Soper, and G. Derbyshire, "Aerodynamic laser-heated contactless furnace for neutron scattering experiments at elevated temperatures," Rev. Sci. Instrum. **71**, 1745–1751 (2000).

[23]L. Hennet, I. Pozdnyakova, A. Bytchkov, V. Cristiglio, P. Palleau, H. E. Fischer, G. J. Cuello, M. Johnson, P. Melin, D. Zanghi, S. Brassamin, J.-F. Brun, D. L. Price, and M.-L. Saboungi, "Levitation apparatus for neutron diffraction investigations on high temperature liquids," Rev. Sci. Instrum. **77**, 053903 (2006).

[24]C. Landron and L. Hennet, "Aerodynamic levitation: A new opportunity in non-destructive characterization at high temperature," AIP Conf. Proc. **497**, 675–680 (1999).

[25]S. Krishnan and D. L. Price, "X-ray diffraction from levitated liquids," J. Phys.: Condens. Matter **12**, 145–176 (2000).

[26]L. B. Skinner, A. C. Barnes, P. S. Salmon, L. Hennet, H. E. Fischer, C. J. Benmore, S. Kohara, J. K. R. Weber, A. Bytchkov, M. C. Wilding, J. B. Parise, T. O. Farmer, I. Pozdnyakova, S. K. Tumber, and K. Ohara, "Joint diffraction and modeling approach to the structure of liquid alumina," Phys. Rev. B **87**, 024201 (2013).

[27]L. Hennet, I. Pozdnyakova, V. Cristiglio, G. J. Cuello, S. Jahn, S. Krishnan, M.-L. Saboungi, and D. L. Price, "Short- and intermediate-range order in levitated liquid aluminates," J. Phys.: Condens. Matter **19**, 455210 (2007).

[28]D. Langstaff, M. Gunn, G. N. Greaves, A. Marsing, and F. Kargl, "Aerodynamic levitator furnace for measuring thermophysical properties of refractory liquids," Rev. Sci. Instrum. **84**, 124901 (2013).

[29]J. Kozaily, L. Hennet, H. E. Fischer, M. Koza, S. Brassamin, S. Magazù, and F. Kargl, "Time–of–flight neutron spectroscopy: A new application of aerodynamic sample levitation," Phys. Status Solidi C **8**, 3155–3158 (2011).

[30]T. C. Hansen, P. F. Henry, H. E. Fischer, J. Torregrossa, and P. Convert, "The D20 instrument at the ill: A versatile high-intensity two-axis neutron diffractometer," Meas. Sci. Technol. **19**, 034001 (2008).

[31]J. A. Rodríguez-Velamazán, J. Campo, J. Rodríguez-Carvajal, and P. Noguera, "XtremeD—A new neutron diffractometer for high pressures and magnetic fields at ill developed by Spain," J. Phys.: Conf. Ser. **325**, 012010 (2011).

[32]J.-M. Zanotti, S. Rodrigues, P. Lavie, P. Permingeat, B. Homatter, and Q. Berrod, "The time-focusing neutron spectrometer sharp," Nucl. Instrum. Methods Phys. Res., Sect. A **1084**, 171196 (2026).

[33]D. Le Maux, M. Courtois, T. Pierre, B. Lamien, and P. Le Masson, "Density measurement of liquid 22MnB5 by aerodynamic levitation," Rev. Sci. Instrum. **90**, 074904 (2019).
[34]G. N. Greaves, M. C. Wilding, S. Fearn, D. Langstaff, F. Kargl, S. Cox, Q. V. Van, O. Majérus, C. J. Benmore, R. Weber, C. M. Martin, and L. Hennet, "Detection of first-order liquid/liquid phase transitions in yttrium oxide–aluminum oxide melts," Science **322**, 566–570 (2008).
[35]J. Ding and W. Ye, "A fast integral approach for drag force calculation due to oscillatory slip stokes flows," Int. J. Numer. Methods Eng. **60**, 1535–1567 (2004).
[36]V. Klapczynski, D. Le Maux, M. Courtois, E. Bertrand, and P. Paillard, "Surface tension measurements of liquid pure iron and 304L stainless steel under different gas mixtures," J. Mol. Liq. **350**, 118558 (2022).
[37]F. Kargl, C. Yuan, and G. N. Greaves, "Aerodynamic levitation: Thermophysical property measurements of liquid oxides," Int. J. Microgravity Sci. Appl. **32**, 320212 (2015).
[38]A. J. Campbell, "Measurement of temperature distributions across laser heated samples by multispectral imaging radiometry," Rev. Sci. Instrum. **79**, 015108 (2008).
[39]S. J. McCormack, A. Tamalonis, R. J. K. Weber, and W. M. Kriven, "Temperature gradients for thermophysical and thermochemical property measurements to 3000 °C for an aerodynamically levitated spheroid," Rev. Sci. Instrum. **90**, 015109 (2019).
[40]S. Krishnan, J. J. Felten, J. E. Rix, J. K. R. Weber, P. C. Nordine, M. A. Beno, S. Ansell, and D. L. Price, "Levitation apparatus for structural studies of high temperature liquids using synchrotron radiation," Rev. Sci. Instrum. **68**, 3512–3518 (1997).
[41]A. Kuball, B. Bochtler, O. Gross, V. Pacheco, M. Stolpe, S. Hechler, and R. Busch, "On the bulk glass formation in the ternary Pd–Ni–S system," Acta Mater. **158**, 13–22 (2018).
[42]J. Sutherland, K.-U. Hess, T. Bissbort, S. Stapperfend, A. Müller, T. C. Hansen, A. Rack, and D. B. Dingwell, "Volatile loss during heating of lunar mare simulants and related compositions," Chem. Geol. **698**, 123115 (2025).
[43]M. Rahimi Chegeni, W. Ma, S. S. Riegler, A. Ghavimi, M. Rohde, F. Yang, H. J. Seifert, I. Gallino, and R. Busch, "Thermodynamic analysis and modeling of Pd–Ni–S bulk metallic glass-forming system," Acta Mater. **294**, 121074 (2025).
[44]J. Wilden, F. Yang, G. Günther, M. Russina, A. Kuball, R. Busch, and A. Meyer, "Ni self-diffusion in glass forming Pd–Ni–S melts," J. Phys.: Condens. Matter **33**, 435101 (2021).
[45]O. Arnold, J. C. Bilheux, J. M. Borreguero, A. Buts, S. I. Campbell, L. Chapon, M. Doucet, N. Draper, R. Ferraz Leal, M. A. Gigg, V. E. Lynch, A. Markvardsen, D. J. Mikkelson, R. L. Mikkelson, R. Miller, K. Palmen, P. Parker, G. Passos, T. G. Perring, P. F. Peterson, S. Ren, M. A. Reuter, A. T. Savici, J. W. Taylor, R. J. Taylor, R. Tolchenov, W. Zhou, and J. Zikovsky, "Mantid—Data analysis and visualization package for neutron and SR experiments," Nucl. Instrum. Methods Phys. Res., Sect. A **764**, 156–166 (2014).
[46]P. Eckstein, D. B. Dingwell, C. H. Thomas, R. Muller Axel, J. Sutherland, and F. Yang, *Laser Sintering Process of Lunar Regolith Simulants Using an Aerodynamic Levitator by Time- and Temperature-Resolved NPD* (Institut Laue-Langevin (ILL), 2024).
[47]P. Eckstein, L. Hennet, A. Mejia Reinoso, S. Savvin, F. Yang, and S. Zimmermann, *Liquid Structure and Crystallization Behaviour of Pd–Ni–S and Pd–Ni–P Glass Forming Alloys Studied Using Aerodynamic Levitation* (Institut Laue-Langevin (ILL), 2024).
[48]P. Eckstein, K. Dammer, A. Meyer, F. Yang, and Z. Jean-Marc, *Correlation Between Thermophysical Properties and Atomic Dynamics in Glass Forming PdNiCuP Liquids* (Institut Laue-Langevin (ILL), 2025).